JACS
JOURNAL OF THE AMERICAN CHEMICAL SOCIETY
pubs.acs.org/JACS
Article

Barocaloric Effects in Dialkylammonium Halide Salts

Jinyoung Seo, Rahil Ukani, Juanjuan Zheng, Jason D. Braun, Sicheng Wang, Faith E. Chen, Hong Ki Kim, Selena Zhang, Catherine Thai, Ryan D. McGillicuddy, Hao Yan,* Joost J. Vlassak,* and Jarad A. Mason*

Cite This: https://doi.org/10.1021/jacs.3c12402

ABSTRACT: Barocaloric effects—solid-state thermal changes induced by the application and removal of hydrostatic pressure—offer the potential for energy-efficient heating and cooling without relying on volatile refrigerants. Here, we report that dialkylammonium halides—organic salts featuring bilayers of alkyl chains templated through hydrogen bonds to halide anions—display large, reversible, and tunable barocaloric effects near ambient temperature. The conformational flexibility and soft nature of the weakly confined hydrocarbons give rise to order−disorder phase transitions in the solid state that are associated with substantial entropy changes (>200 J kg^{-1} K^{-1}) and high sensitivity to pressure (>24 K $kbar^{-1}$), the combination of which drives strong barocaloric effects at relatively low pressures. Through high-pressure calorimetry, X-ray diffraction, and Raman spectroscopy, we investigate the structural factors that influence pressure-induced phase transitions of select dialkylammonium halides and evaluate the magnitude and reversibility of their barocaloric effects. Furthermore, we characterize the cyclability of thin-film samples under aggressive conditions (heating rate of 3500 K s^{-1} and over 11,000 cycles) using nanocalorimetry. Taken together, these results establish dialkylammonium halides as a promising class of pressure-responsive thermal materials.

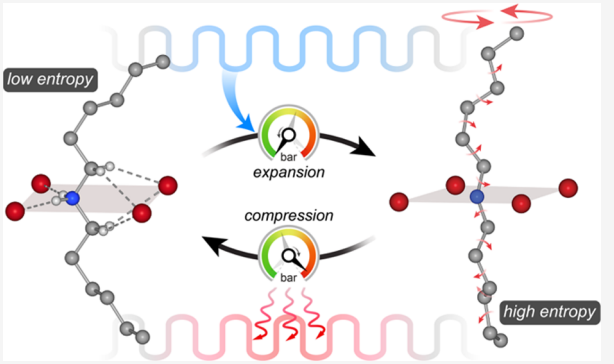

INTRODUCTION

Since the invention of vapor-compression refrigeration nearly two centuries ago,[1−3] cooling technologies have played a critical role in driving economic growth and improving living conditions around the world.[4,5] Indeed, vapor-compression systems are now ubiquitous, with over 4 billion air conditioners, refrigerators, and heat pumps in use throughout the world.[6−8] Nearly all of these systems pump heat against a temperature gradient by expanding and compressing volatile hydrofluorocarbon (HFC) refrigerants—the majority of which are potent greenhouse gases with global warming potentials (GWPs) more than 1000 times that of carbon dioxide.[9] Over 0.4 megatons of these refrigerants leak into the atmosphere each year,[10] which accounts for nearly 3% of global greenhouse gas emissions.[6] As the demand for cooling systems and heat pumps continues to increase,[7,8] the direct emission of HFCs is projected to climb to upward of 20% of greenhouse gas emissions by 2050,[11,12] and replacing high-GWP refrigerants with low-GWP refrigerants—such as hydrofluoroolefins, hydrocarbons, ammonia, or carbon dioxide—often involves complicated trade-offs in efficiency, performance, cost, and safety.[13] Moreover, volatile molecules often react in unexpected ways once they inevitably reach the atmosphere,[14−16] which can have unintended consequences for the environment that are difficult to predict.[17−20] Alternative technologies that do not rely on volatile refrigerants are, thus, urgently needed to enable more sustainable cooling and heating.

Just as compressing and expanding a volatile refrigerant induces a phase transition between a gas and liquid that is accompanied by a large change in entropy and temperature, increasing and decreasing the pressure around a solid material can also induce phase transitions between high- and low-entropy states. Such solid-state transitions can, in principle, be leveraged to pump heat from a low-temperature heat source to a high-temperature heat sink.[21−24] In most solid materials, pressure-induced thermal changes—known as barocaloric effects—are small unless very large pressures (well above 1 kbar) are applied.[25−27] Certain classes of solid-state phase-change materials, however, can exhibit large barocaloric effects at low pressures that provide exciting opportunities for high-efficiency heating and cooling with nonvolatile refrigerants.[28]

Phase transitions between crystalline and dynamically disordered bilayers of hydrocarbon chains in two-dimensional (2D) metal−halide perovskites of the form $[(C_nH_{2n+1}NH_3)_2MX_4]$ (M = Mn, Cu; X = Cl, Br) offer a

Received: November 6, 2023
Revised: December 26, 2023
Accepted: January 2, 2024
Published: January 16, 2024

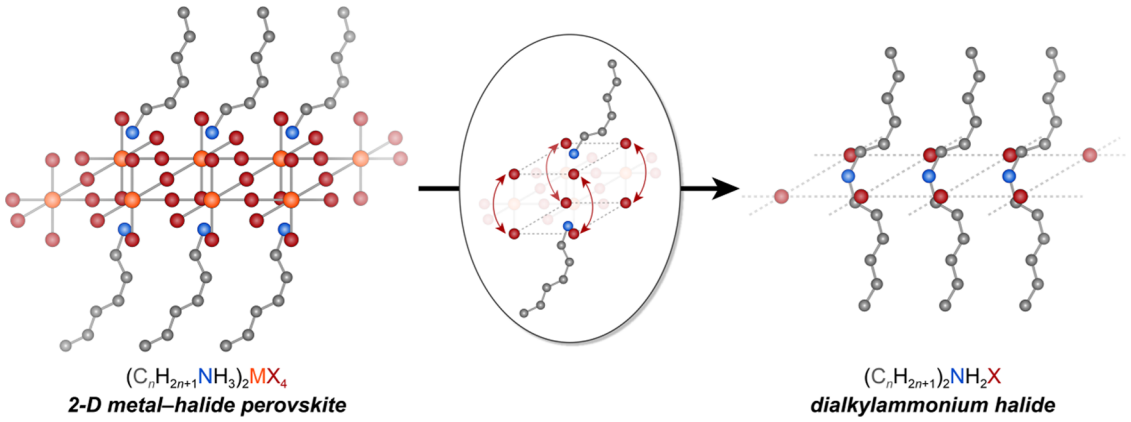

Figure 1. Illustration of how dialkylammonium halide salts template the arrangement of hydrocarbon bilayers in a manner that is analogous to that of two-dimensional metal–halide perovskites. Orange, red, gray, and blue spheres represent transition metal (M), halide (X), C, and N atoms, respectively. H atoms are omitted for clarity.

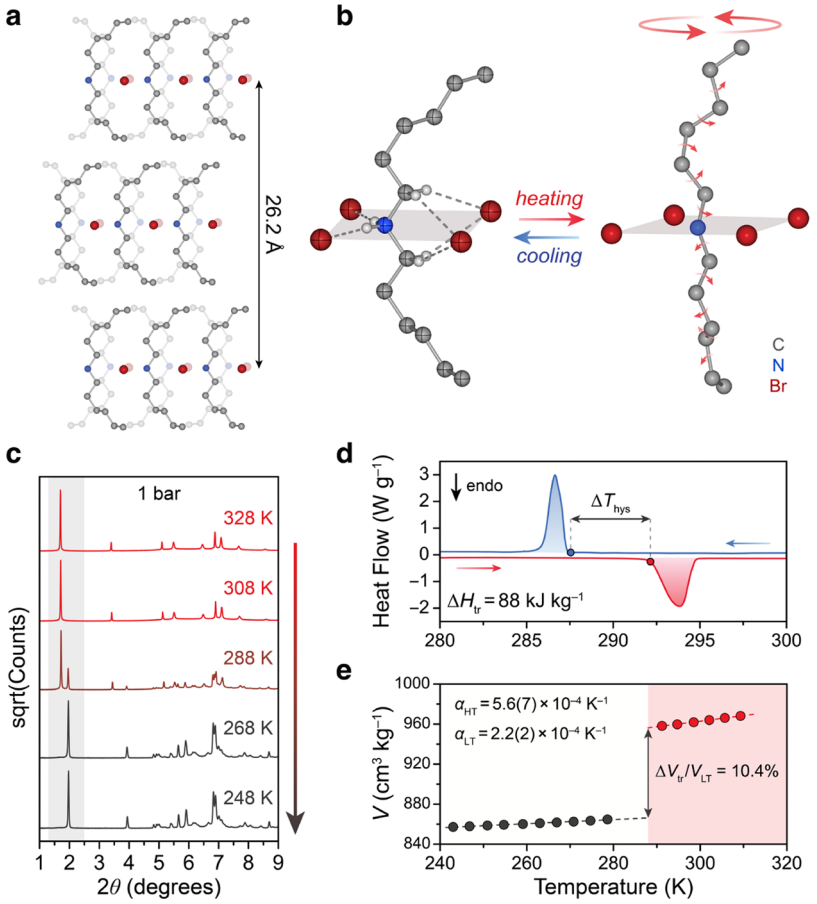

Figure 2. (a) Single-crystal structure of the low-entropy phase of $(C_6H_{13})_2NH_2Br$ obtained at 100 K showing noninterdigitated bilayers of hexyl chains. Gray, blue, and red spheres correspond to the C, N, and Br atoms, respectively. H atoms are omitted for clarity. (b) Thermally induced order–disorder transition of $(C_6H_{13})_2NH_2Br$ involves changes to the conformational and rotational degrees of freedom of the confined dihexylammonium chains. Note that the structure of the ordered phase was obtained from X-ray crystallography (left), while the structure of the disordered phase was calculated by density functional theory (right). (c) Variable-temperature powder X-ray diffraction (PXRD) patterns for $(C_6H_{13})_2NH_2Br$ obtained during cooling under 1 bar of He with an X-ray wavelength of 0.45213 Å. (d) Differential scanning calorimetry (DSC) trace for a powder sample of $(C_6H_{13})_2NH_2Br$ at 1 bar with heating (red) and cooling (blue) rates of 2 K min^{-1}. (e) Specific volumes obtained from variable-temperature PXRD are used to calculate the volume change, ΔV_{tr}, that accompanies the order–disorder transition for $(C_6H_{13})_2NH_2Br$, along with the thermal expansivity (α) of the low-temperature (LT) and high-temperature (HT) phases.

particularly promising mechanism for inducing large, reversible barocaloric effects at low pressures.[29,30] In 2D perovskites, inorganic layers of corner-sharing metal–halide octahedra template the packing of alkylammonium cations and keep the hydrocarbon chains confined to the solid state even when they take on liquid-like vibrational and rotational degrees of freedom in the partially disordered, high-temperature phase.[31] The structural and chemical features of 2D perovskites

https://doi.org/10.1021/jacs.3c12402
J. Am. Chem. Soc. XXXX, XXX, XXX–XXX

are well-suited to promoting strong barocaloric effects: (i) the flexibility of hydrocarbon chains leads to a large number of degenerate configurations within the partially disordered lattice, driving a large phase-change entropy, (ii) the confined nature of the organic bilayer leads to strong coupling between structural degrees of freedom and volume, giving rise to high pressure sensitivity, and (iii) the organic−inorganic and organic−organic interfaces can be tailored to minimize hysteresis.[29] Although the inorganic layers of 2D perovskites offer a unique handle for improving and optimizing materials properties important to high-efficiency barocaloric cooling—including hysteresis, thermal conductivity, and mechanical strength—the metal cations and charge-balancing halide anions within the layers also add substantial weight and volume without directly contributing to the phase-change entropy.

In pursuit of a metal-free platform for solid-state hydrocarbon transitions that produce strong barocaloric effects, we recognized that the organic bilayers within dialkylammonium halide salts of the form $(C_nH_{2n+1})_2NH_2X$ [denoted here as $(C_n)_2X$ where X = Cl, Br, I] adopt structures that are analogous to those of 2D perovskites. As illustrated in Figure 1, the structure of $(C_n)_2X$ can be derived from $(C_nH_{2n+1}NH_3)_2MX_4$ without altering the overall hydrocarbon chain packing simply by removing the metal cations and merging axially adjacent ammonium groups and halides. Similar to 2D perovskites, dialkylammonium halides thus feature bilayers of hydrocarbon chains that are confined through hydrogen bonding interactions with 2D sheets of halide anions and can undergo reversible solid-state order−disorder transitions. Although the phase-change thermodynamics of many dialkylammonium halides has been investigated in detail at ambient pressure in the context of thermal energy storage,[32−34] the structural information available for this class of compounds is limited, making it challenging to gain mechanistic insights into their phase transitions and to establish structure−property relationships.[32,35,36] In addition, the effect of pressure on dialkylammonium halide phase transitions has not yet been investigated, though we note a somewhat similar compound (di-*n*-butylammonium tetrafluoroborate) was recently reported to exhibit large barocaloric effects.[37] Herein, we report a detailed investigation of barocaloric effects in symmetric dialkylammonium halide salts and demonstrate that, when appropriately designed, these materials exhibit properties that make them promising solid refrigerants.

RESULTS AND DISCUSSION

Solid-State Phase Transitions at Ambient Pressure. To begin investigating barocaloric effects in dialkylammonium halide salts, we selected $(C_6)_2Br$ [$(C_6)_2$ = di-*n*-hexylammonium] as a representative compound known to undergo a high-entropy phase transition near ambient temperature.[34] Specifically, an order−disorder transition occurs in $(C_6)_2Br$ at a transition temperature, T_{tr}, of 293 K with an associated entropy change, ΔS_{tr}, of 300 J K^{-1} kg^{-1} (315 J K^{-1} L^{-1}) and an enthalpy change, ΔH_{tr}, of 88 kJ kg^{-1} (92 kJ L^{-1}) (Figure 2d). As anticipated, the magnitude of these entropy and enthalpy changes exceeds those of analogous 2D perovskites on both a gravimetric and volumetric basis (Table S1). Interestingly, the molar ΔS_{tr} of $(C_6)_2Br$ (80 J mol^{-1} K^{-1}) is more than twice as large as that of $(C_6H_{13}NH_3)_2MnCl_4$ (37 J mol^{-1} K^{-1})[38] even though both compounds undergo transitions near 292 K. This can be partially attributed to a minor disordering transition that $(C_6H_{13}NH_3)_2MnCl_4$ undergoes at much lower temperatures,[38] though the total hydrocarbon order−disorder transition entropy is still 21% lower for the 2D perovskite compared to $(C_6)_2Br$. This could result from a gradual change in hydrocarbon degrees of freedom for $(C_6H_{13}NH_3)_2MnCl_4$ outside of the first-order phase-transition regions or could reflect an intrinsic difference in the overall entropy change that may arise from differences in chain packing and confinement effects.[32]

To gain additional insight into the structural nature of the $(C_6)_2Br$ phase transition, we performed a series of variable-temperature X-ray diffraction experiments. Despite the extensive investigations of their thermal properties, the only crystal structure previously reported for a dialkylammonium halide salt was, to the best of our knowledge, of $(C_{18})_2Br$ at 288 K.[36] Here, the structure of $(C_6)_2Br$ in the low-temperature phase was determined by single-crystal X-ray diffraction at 100 K (Figures 2a and S10). In this monoclinic ($C2/c$) phase, the dihexylammonium cations pack into noninterdigitated bilayers with an interlayer spacing of 13.1 Å. Each ammonium cation is confined by charge-assisted hydrogen bonds to four coplanar Br anions in a square planar arrangement. Note that the confinement area of the Br anions is 28.7 $Å^2$ (Figure S8 and Table S2), which matches the area for the plane of axial Br anions in Cu−Br perovskites (29 $Å^2$).[29] In addition, the electron-deficient carbon atoms (C1 and C1′) adjacent to the ammonium center also contribute to chain confinement by engaging in ion−dipole (Br···H−C) interactions. The two hexyl chains, which are oriented out of the Br plane with a dihedral angle of 72.8°, are tilted 43.5° with respect to the Br plane and have a single gauche C2−C3 bond (torsion angle of 65°) among trans C−C bonds (torsion angle of ∼180°) (Table S4). Again, these structural features are similar to those observed in Cu−Br perovskites that also display a tilt angle of 41−43° and a gauche C2−C3 bond at low temperatures.[29]

Attempts to determine the crystal structure of $(C_6)_2Br$ above the phase transition temperature were unsuccessful owing to the high mechanical flexibility of the partially disordered crystal. Indeed, AFM force spectroscopy revealed that the elastic modulus of $(C_6)_2Br$ at 300 K is only 0.6 GPa (Figure S54). Nonetheless, variable-temperature powder X-ray diffraction (PXRD) experiments show that $(C_6)_2Br$ transitions to an expanded tetragonal phase ($I4/mmm$) at high temperatures with a large volume change (ΔV_{tr}) of 10.4% (Figure 2c,2e). The volume change is highly anisotropic, largely occurring through a 13.4% increase in the interlayer distance (Figure S18). The coefficient of thermal expansion (α) for the high-temperature phase ($5.6(7) \times 10^{-4}$ K^{-1}) is notably larger than for the low-temperature phase ($2.2(2) \times 10^{-4}$ K^{-1}), indicating that strong anharmonicity is present in the disordered hydrocarbons—similar to the rotator phases of *n*-alkanes.[39] In addition, there is a large contribution from diffuse scattering to the PXRD patterns of the high-temperature phase, which is consistent with the presence of substantial dynamic disorder (Figures 2c and S28). In fact, previous solid-state NMR studies have suggested that dialkylammonium cations in shorter-chain analogues of $(C_n)_2Br$ (n = 2, 3, 4) rotate along the principal chain axis in the high-temperature phase, behaving as low-dimensional plastic crystals.[35]

In the absence of an experimental crystal structure, we used density functional theory (DFT) calculations to model the high-temperature structure of $(C_6)_2Br$ with the 100-K single-

https://doi.org/10.1021/jacs.3c12402
J. Am. Chem. Soc. XXXX, XXX, XXX−XXX

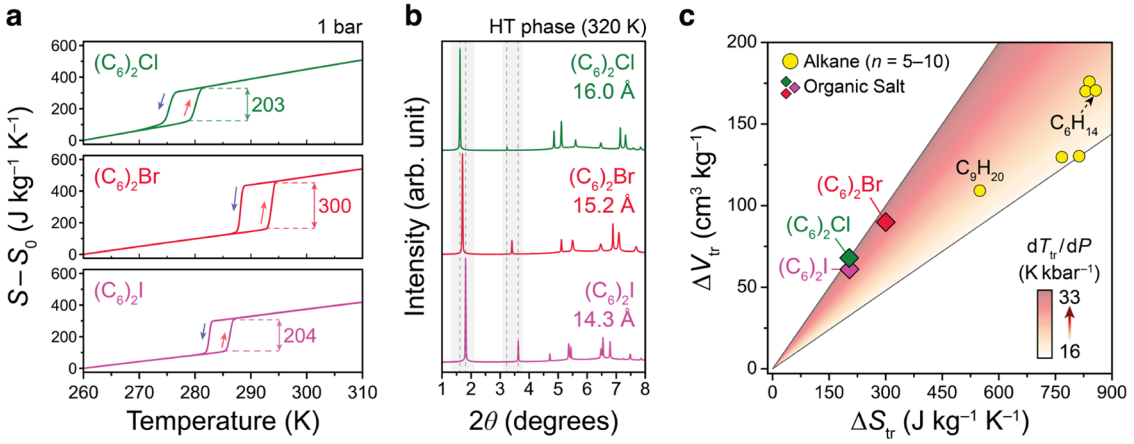

Figure 3. (a) Isobaric entropy curves for $(C_6H_{13})_2NH_2X$ (X = Cl, Br, I) are plotted as a function of temperature at ambient pressure for heating and cooling transitions. Phase-change entropy values are denoted on the plot in units of J kg^{-1} K^{-1}. Note that the entropy reference state (S_0) corresponds to the entropy at 260 K. (b) PXRD patterns for high-temperature (HT) phases at 320 K along with the corresponding interlayer spacings. (c) Comparison of transition entropy changes (ΔS_{tr}) and volume changes (ΔV_{tr}) for hydrocarbon solid−solid transitions in dialkylammonium halides (diamond symbols) to melting transitions in *n*-alkanes (circles). The pressure sensitivity of each phase transition is calculated by using the Clausius−Clapeyron relationship, and the magnitude is indicated by shading from light yellow (low dT_{tr}/dP) to brown (high dT_{tr}/dP).

crystal structure serving as a starting point and adjusting the unit-cell dimensions to match those determined from PXRD at 330 K. In the resulting DFT model structure, which represents a snapshot of a potential local energy minimum in the partially disordered phase, the tilt angles of the hexyl groups increase to above 60° relative to the Br plane as the chains undergo conformational changes (Figure 2b). Specifically, the hydrocarbon chains now have an additional gauche C3−C4 bond, along with small distortions (0−30°) in the trans C−C bonds across the rest of the chain (Table S4). The hydrocarbon chains are also engaged in weaker hydrogen bonds, as indicated by a Hirshfeld surface analysis showing elongated and distorted N−H···Br and C−H···Br contacts (Figure S9). Still, the square planar Br anions remain largely intact around the ammonium centers with minimal change in Br−Br distances (Figure S8). The presence of in-plane hydrogen bonding in the high-temperature phase is further supported by absorption bands near 2800−3000 cm^{-1} in the infrared spectrum (Figure S4), which can be assigned to red-shifted N−H stretching vibrations.[40−42] Overall, these results suggest that hydrogen bonding between ammonium chains and Br anions persists in the high-temperature phase and imparts a degree of long-range order, highlighting the critical roles of halide anions in governing the internal degrees of freedom of the confined chains.

Further insight into the structural and chemical factors that influence phase-change thermodynamics can be gained by examining the effects of halide substitution, which has a direct impact on chain confinement as demonstrated in 2D perovskites.[29,43] Similar to $(C_6)_2Br$, the Cl analogue $(C_6)_2Cl$, which was previously reported but not structurally characterized,[32] and I analogue $(C_6)_2I$ undergo reversible solid−solid transitions below room temperature at 279 and 286 K, respectively (Figure 3a). Interestingly, the molar entropy changes of both compounds [45 J K^{-1} mol^{-1} for $(C_6)_2Cl$ and 64 J K^{-1} mol^{-1} for $(C_6)_2I$] are lower than that for $(C_6)_2Br$. Note that $(C_6)_2Cl$ has a minor phase transition at 115 K with a small ΔS_{tr} of 8 J K^{-1} mol^{-1}, which has been attributed to the onset of rotation of the dihexylammonium cations.[32]

We tentatively hypothesize that Br anions lead to the highest entropy change within the $(C_6)_2X$ (X = Cl, Br, I) series because the ammonium confinement area is large enough to maximize hydrocarbon degrees of freedom in the high-temperature phase but small enough to prevent the hydrocarbons from partially disordering in the low-temperature phase. A single-crystal structure obtained at 100 K confirms that the area of the Cl plane is 13% smaller than that for the Br analogue (Figure S12 and Table S3). Moreover, the interlayer spacing decreases with increasing halide size in the high-temperature phase from 16.0 Å (Cl) to 14.3 Å (I; Figure 3b). This trend—also observed in 2D perovskites[29,43]—arises because the dihexyl chains adopt smaller tilt angles to maximize van der Waals interactions between chains as the area of the halide plane increases. Note that F analogues of $(C_6)_2X$ do not undergo solid−solid transitions because the F anions are too small (r_F = 1.33 Å) to accommodate disordered dialkylammonium cations that have rotational diameters on the order of 4−5 Å.[33]

Consistent with their smaller entropy changes, the $(C_6)_2Cl$ and $(C_6)_2I$ phase transitions are also associated with smaller—though similarly anisotropic—volume changes of 6.5 and 7.8%, respectively (Figures S16 and S17). The experimentally determined volume and entropy changes can be used to estimate the pressure dependence of the transition temperature, dT_{tr}/dP, through the Clausius−Clapeyron relationship ($dT_{tr}/dP = \Delta V_{tr}/\Delta S_{tr}$). Also termed the barocaloric coefficient, the magnitude of dT_{tr}/dP is a critical determinant of the performance and operating conditions of a barocaloric material as it dictates how large of of a pressure shift (ΔP) is needed to induce a given thermal change (ΔT). As dictated by the Clausius−Clapeyron relation, dT_{tr}/dP is highest when ΔS_{tr} is small and ΔV_{tr} is large. The inverse relationship between ΔS_{tr} and dT_{tr}/dP represents a challenge for barocaloric materials given the importance of maximizing both ΔS_{tr} and dT_{tr}/dP. Owing to their large ΔV_{tr}, the phase transitions for all three dialkylammonium halide compounds studied here are predicted to exhibit high sensitivity to pressure, with calculated barocaloric coefficients of 33, 30, and 30 K kbar^{-1} for Cl, Br, and I analogues, respectively (Figure 3c). These values are

https://doi.org/10.1021/jacs.3c12402
J. Am. Chem. Soc. XXXX, XXX, XXX−XXX

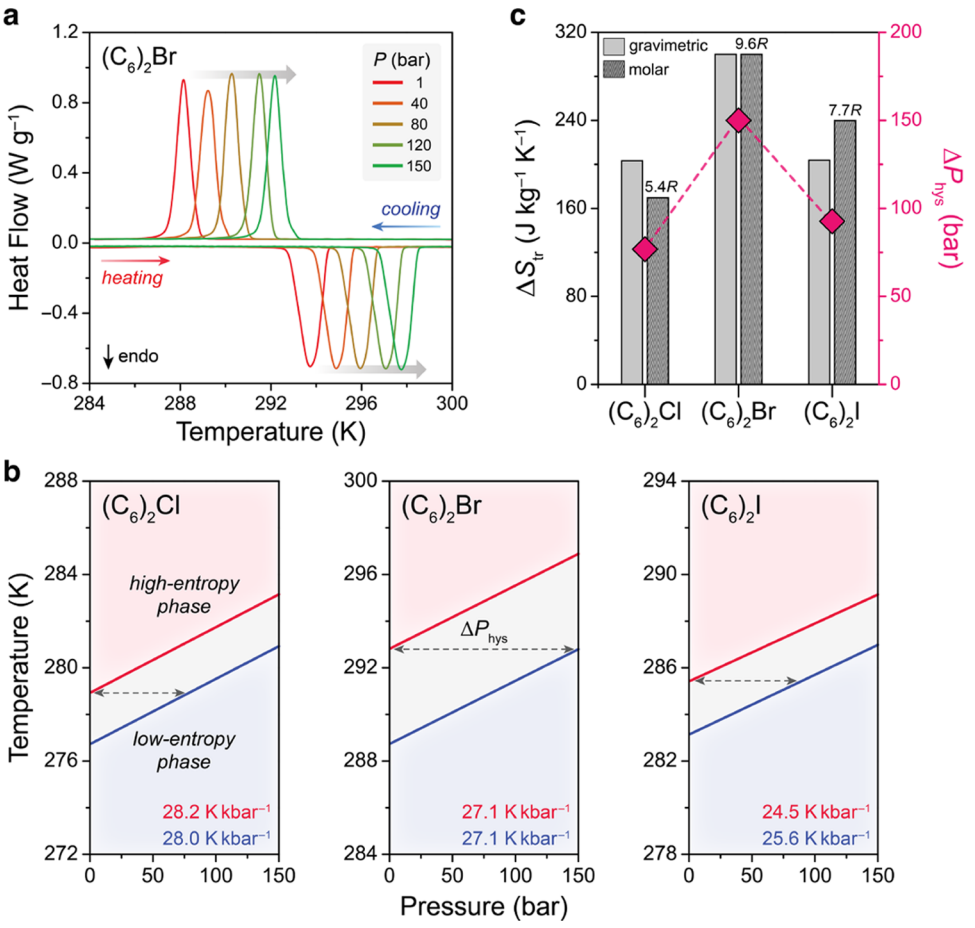

Figure 4. (a) Isobaric HP-DSC measurements for $(C_6)_2Br$ with heating and cooling rates of 0.5 K min^{-1}. (b) Pressure−temperature (P, T) phase diagrams for $(C_6)_2X$ showing phase boundaries for heating (red) and cooling (blue), with the hysteresis region highlighted in gray. (c) Relationship between phase-change entropy (ΔS_{tr}) and pressure hysteresis (ΔP_{hys}). The ΔP_{hys} values were calculated from the experimentally determined thermal hysteresis (ΔT_{hys}) and pressure sensitivity (dT_{tr}/dP).

comparable to some of the highest coefficients reported for barocaloric materials of any type (Table S10 and Figure S52) and are larger than those associated with melting transitions in *n*-alkanes (20 K kbar^{-1}).[44,45] We note that the higher pressure sensitivity compared to *n*-alkanes results from the lower relative ΔS_{tr} of dialkylammonium halides rather than a difference in ΔV_{tr}.

Pressure−Temperature Phase Diagram. To experimentally probe barocaloric effects in $(C_6)_2X$, we performed isobaric high-pressure differential scanning calorimetry (HP-DSC) measurements using He as the pressure-transmitting medium. In these experiments, phase transition temperatures—as well as enthalpies and entropies—were determined as a function of pressure up to 150 bar (Figure 4a). The resulting pressure−temperature (P−T) diagrams reveal phase boundaries that allow pressure sensitivity and hysteresis to be evaluated (Figure 4b). As summarized in Figure 4b, the dT_{tr}/dP values for $(C_6)_2X$ are 28 K kbar^{-1} (Cl), 27 K kbar^{-1} (Br), and 25 K kbar^{-1} (I). These measured pressure sensitivities are 84% (Cl), 90% (Br), and 84% (I) of those predicted from the Clausius−Clapeyron relationship (Table S6). The small decrease in experimental pressure sensitivity is attributed to He penetration into the disordered organic bilayer of the high-temperature phase.[29,39]

Hysteresis represents an additional energy barrier that must be overcome in order to drive first-order phase transitions in a reversible manner,[46,47] leading to dissipation of input energy that negatively impacts efficiency, power, and material longevity.[24,28,48−50] As illustrated in Figure 4b, $(C_6)_2Br$ has a thermal hysteresis (ΔT_{hys}) of 4 K, whereas $(C_6)_2Cl$ and $(C_6)_2I$ exhibit a lower ΔT_{hys} of 2 K. In addition to thermal hysteresis, pressure hysteresis (ΔP_{hys}) (defined as the difference in onset pressures between compression- and expansion-induced transitions) is an important metric for evaluating barocaloric materials. On a P−T phase diagram, ΔP_{hys} corresponds to the horizontal width of the hysteresis region defined by cooling and heating boundaries and thus can be calculated from ΔT_{hys} and dT_{tr}/dP as

$$\frac{dT_{tr}}{dP} = \frac{\Delta T_{hys}}{\Delta P_{hys}} \quad (1)$$

Using eq 1, ΔP_{hys} was calculated to be 76 bar (Cl), 149 bar (Br), and 98 bar (I). Since phase transitions of real materials are not perfectly sharp—occurring over a range of pressures rather than a single pressure—ΔP_{hys} represents the minimum pressure required to begin to induce a thermodynamically reversible barocaloric effect,[48] but higher pressures will be required to induce a large enough reversible temperature and entropy change to drive a practical cooling or heating cycle. Importantly, the ΔP_{hys} values for the dialkylammonium halide salts are below 150 bar, which are among the lowest pressure

https://doi.org/10.1021/jacs.3c12402
J. Am. Chem. Soc. XXXX, XXX, XXX−XXX

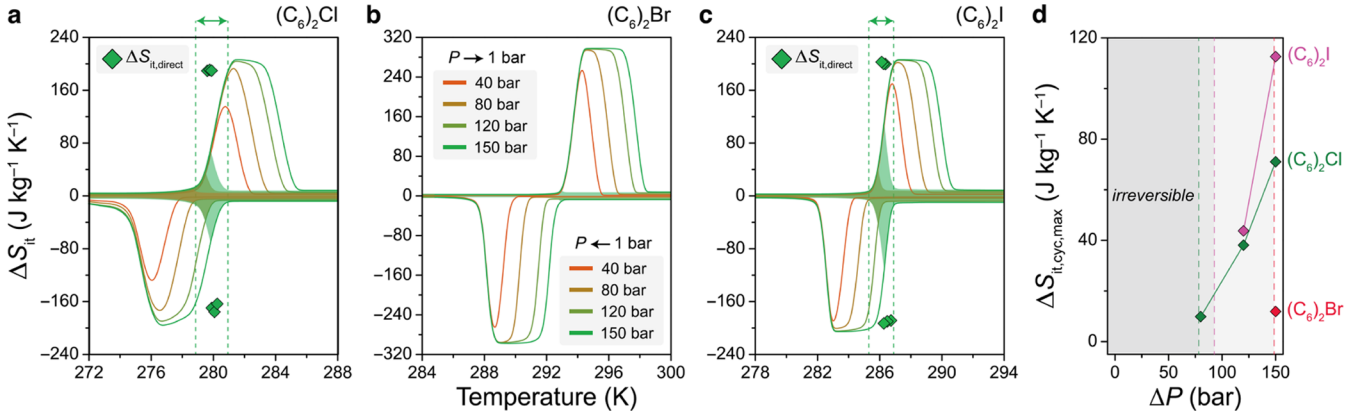

Figure 5. (a–c) Isothermal entropy changes (ΔS_{it}) calculated via the quasi-direct method for (a) $(C_6)_2Cl$, (b) $(C_6)_2Br$, and (c) $(C_6)_2I$. The shaded area indicates the cyclable isothermal entropy change ($\Delta S_{it,cyc}$) that is accessible for each operating pressure. The temperature window over which a nonzero $\Delta S_{it,cyc}$ is possible at 150 bar is indicated by green dashed lines. $\Delta S_{it,direct}$ values measured from quasi-isothermal DSC experiments are shown as green diamonds for comparison. (d) Maximum cyclable isothermal entropy change ($\Delta S_{it,cyc,max}$) calculated from isobaric HP-DSC measurements is plotted against operating pressure (ΔP). ΔP_{hys} values determined from isobaric HP-DSC are shown as dashed lines for $(C_6)_2Cl$ (green), $(C_6)_2Br$ (red), and $(C_6)_2I$ (purple).

hysteresis values that have been reported for barocaloric materials (Table S10). Moreover, it is worth highlighting that dialkylammonium halides, along with 2D perovskites, represent one of few barocaloric material classes that feature a combination of large entropy changes (>200 J K^{-1} kg^{-1}) and low pressure hysteresis (<150 bar) (Figure S51).

Interestingly, as shown in Figure 4c, the calculated ΔP_{hys} values are correlated with ΔS_{tr}, suggesting that there may be a trade-off between the reversibility and magnitude of barocaloric effects in $(C_6)_2X$. Although ΔS_{tr} also appears to be correlated with ΔV_{tr} (Figure 3c), more detailed investigations into geometric phase compatibility are needed to provide insight into the entropy–hysteresis correlation and to better understand the influence of overall volume change and interfacial strain on phase-change reversibility.[51] More broadly, investigations into nucleation mechanisms—at both molecular and microstructural levels—will be required to understand the origin of hysteresis and to help establish design principles for simultaneously maximizing entropy changes and minimizing hysteresis across hydrocarbon order–disorder transitions. Such design principles, which have received limited attention in the barocaloric field, will play a critical role in advancing the basic science needed to support practical applications of barocaloric materials.

Evaluation of Barocaloric Effects. To evaluate barocaloric effects in $(C_6)_2X$ (X = Cl, Br, I), we first constructed isothermal entropy curves through the so-called quasi-direct method.[52] In this approach, isobaric entropy curves, $S_{ib}(P, T)$, are calculated from heat flow and heat capacity data obtained from isobaric DSC measurements (Figures S30–S34). Isothermal entropy curves, ΔS_{it}, which describe entropy changes induced by a shift in pressure as a function of temperature, are then obtained by subtracting the isobaric entropy curves at two different pressures. For the disordering transition that is induced by decompression from applied pressure P to ambient pressure P_0, the ΔS_{it} curve is calculated from S_{ib} curves associated with heating transitions as

$$\Delta S_{it}(P \rightarrow P_0) = S_{ib,heating}(T, P_0) - S_{ib,heating}(T, P) \quad (2)$$

Similarly, for the compression-induced ordering transition, S_{ib} curves obtained from cooling transitions are used to calculate the ΔS_{it} curve with

$$\Delta S_{it}(P_0 \rightarrow P) = S_{ib,cooling}(T, P) - S_{ib,cooling}(T, P_0) \quad (3)$$

The resulting ΔS_{it} curves for $(C_6)_2X$ (X = Cl, Br, I) illustrate the impact of hysteresis on accessing reversible barocaloric effects (Figure 5a–c). Specifically, cyclable isothermal entropy changes ($\Delta S_{it,cyc}$) can be induced for $(C_6)_2Cl$ and $(C_6)_2I$ at a 150 bar operating pressure over a temperature range of 2 K. In contrast, compression and decompression ΔS_{it} curves for $(C_6)_2Br$ do not overlap below 150 bar because of a larger pressure hysteresis of 149 bar (Figure 5b). The lack of overlap in ΔS_{it} curves indicates that there is no temperature range over which $\Delta S_{it,cyc}$ can be induced from a cyclic change in pressure. At 150 bar, there is a small region of overlap in the ΔS_{it} curves, yielding a maximum entropy change of 12 J K^{-1} kg^{-1} over an extremely narrow temperature range of around 293 K (Figure 5d).

Although a 150 bar driving pressure is above the pressure hysteresis for $(C_6)_2X$, the maximum entropy changes accessible at 150 bar are still lower than the full ΔS_{tr} values (Figure 5d), indicating that $\Delta S_{it,cyc}$ arises from partial phase transformations. This is because first-order phase transitions are associated with a finite peak width (ΔT_{width}). To access the full phase-change entropy, a hysteresis loop created between heating and cooling entropy curves at an applied pressure needs to be fully separated from a hysteresis loop at ambient pressure to an extent that the temperature shift in the hysteresis loop surpasses the combination of ΔT_{hys}, $\Delta T_{width,heating}$, and $\Delta T_{width,cooling}$. Such a pressure, denoted as $\Delta P_{rev,full}$, can be estimated from dT_{tr}/dP as

$$\frac{dT_{tr}}{dP} = \frac{\Delta T_{hys} + \Delta T_{width,heating} + \Delta T_{width,cooling}}{\Delta P_{rev,full}} \quad (4)$$

Above $\Delta P_{rev,full}$, reversible adiabatic temperature changes also become accessible.[48] Assuming that dT_{tr}/dP and ΔT_{hys} are relatively constant at higher pressures, the quasi-direct analysis suggests that $\Delta P_{rev,full}$ of 253, 257, and 200 bar are required to fully overcome hysteresis for $(C_6)_2Cl$, $(C_6)_2Br$, and $(C_6)_2I$, respectively. Note that the maximum possible magnitudes of

https://doi.org/10.1021/jacs.3c12402
J. Am. Chem. Soc. XXXX, XXX, XXX–XXX

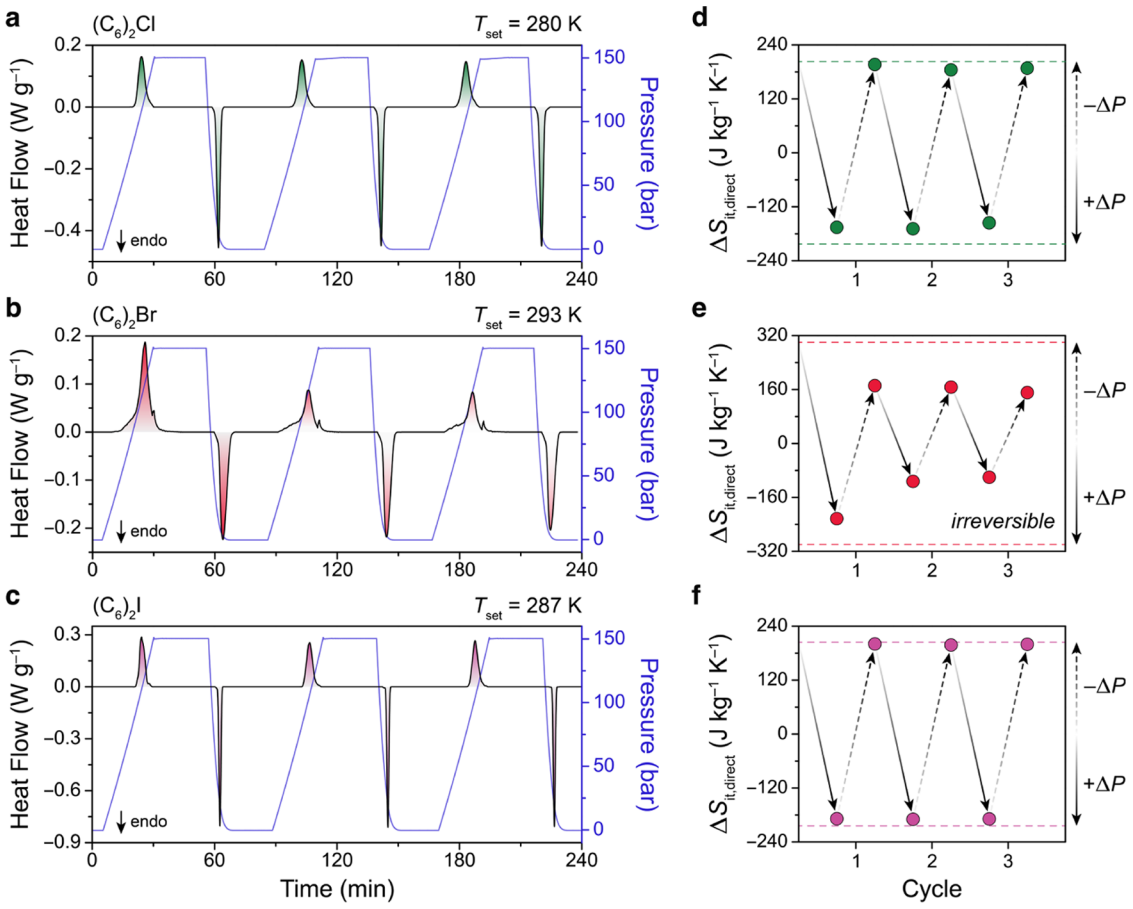

Figure 6. (a–c) Direct evaluation of pressure-induced hydrocarbon transitions through isothermal DSC experiments for (a) $(C_6)_2Cl$, (b) $(C_6)_2Br$, and (c) $(C_6)_2I$. Heat flow signals were recorded during three cycles of applying and removing a hydrostatic pressure of 150 bar with He as the pressure-transmitting medium. The pressure was increased linearly at a rate of 6 bar min^{-1} and decreased asymptotically at an average rate of 13 bar min^{-1}. (d–f) Isothermal entropy changes from pressure-swing DSC ($\Delta S_{it,direct}$) are plotted over three pressure cycles for (d) $(C_6)_2Cl$, (e) $(C_6)_2Br$, and (f) $(C_6)_2I$. $\Delta S_{it,direct}$ values were calculated using $\Delta S_{it,direct} = q_{it}/T_{set}$, where q_{it} represents the area under the heat flow peak and T_{set} represents the set temperature for the pressure swing, respectively.

adiabatic temperature changes ($\Delta T_{ad,max}$) can be estimated using the indirect calculation $\Delta T_{ad,max}(T) = -T\Delta S_{it,max}/c_p$, where c_p is the ambient-pressure heat capacity and $\Delta S_{it,max}$ is the maximum isothermal entropy change. $\Delta T_{ad,max}$ values for $(C_6)_2X$ are 33 K (Cl), 59 K (Br), and 45 K (I), which—assuming constant dT_{tr}/dP—would require operating pressures of at least 1150, 2187, and 1842 bar, respectively.

Although the quasi-direct analysis offers a facile method to estimate barocaloric properties, this approach inherently relies on phase-change properties measured for thermally induced transitions rather than pressure-induced transitions. As such, this can be misleading. For instance, the measurement of transition hysteresis and peak width—kinetic factors that directly influence reversible barocaloric effects—using isobaric HP-DSC can be influenced by extrinsic factors, such as the sample environment, scan rate, and thermal contact.[29,46]

Quasi-Isothermal Pressure-Swing DSC. To more directly evaluate barocaloric effects in $(C_6)_2X$ (X = Cl, Br, I), we carried out quasi-isothermal, pressure-swing DSC measurements (Figure 6a–f). In these experiments, heat flow signals were measured as the hydrostatic pressure was continuously shifted between 1 and 150 bar. Although the use of He gas as the pressure-transmitting medium led to small temperature fluctuations (ΔT_{avg} < 0.2 K) during pressure cycling (Figures S38–S40), the sample temperature stabilized to within 0.4 K of the transition onset, indicating that quasi-isothermal conditions were maintained (Table S9). By capturing the compression-induced exotherms and decompression-induced endotherms, pressure-swing DSC enables the direct characterization of phase-change thermodynamics under more realistic conditions. Throughout the pressure swing, the sample temperature was set to about 1 K above the ambient-pressure $T_{tr,heating}$ (Figure S41). These set temperatures, T_{set}, were selected based on the P–T diagrams and isothermal entropy curves to ensure that reversible transitions were accessible below 150 bar. From the isothermal cycling data, the amount of heat absorbed and released during the pressure swing, q_{it}, were obtained by integrating the endotherms and exotherms. Using q_{it}, isothermal entropy changes, $\Delta S_{it,direct}$, were then calculated as $\Delta S_{it,direct} = q_{it}/T_{set}$. Note that the experimental $\Delta S_{it,direct}$ values tend to exceed the isothermal entropy changes calculated from the isobaric data because the temperature fluctuation during the pressure swing contributes to driving the phase transitions toward completion.[53]

As shown in Figure 6d,6f, pressure-induced phase transitions in $(C_6)_2Cl$ and $(C_6)_2I$ were reversible with $\Delta S_{it,direct}$ nearly approaching the full transition entropy: 82% (compression) and 93% (decompression) of ΔS_{tr} for $(C_6)_2Cl$ (163–190 J K^{-1} kg^{-1}), and 92% (compression) and 98% (decompression) of ΔS_{tr} for $(C_6)_2I$ (189–200 J K^{-1} kg^{-1}). Note that the

https://doi.org/10.1021/jacs.3c12402
J. Am. Chem. Soc. XXXX, XXX, XXX–XXX

compression $\Delta S_{it,direct}$ values were consistently smaller than the decompression $\Delta S_{it,direct}$, which can likely be attributed to a larger dissipation of heat signals during the slower compression step (6 bar min^{-1}) than during decompression (13 bar min^{-1}). Significantly, the $\Delta S_{it,direct}$ values remained unchanged over the three cycles, demonstrating that the 150 bar pressure swing provides a sufficient thermodynamic driving force for $(C_6)_2Cl$ and $(C_6)_2I$ to reversibly transition between low-entropy and high-entropy phases. Overall, these results are in agreement with the ΔS_{it} curves calculated from isobaric HP-DSC measurements (Figure 5a,5c), directly validating the reversible temperature window predicted from the quasi-direct analysis.

By contrast, $(C_6)_2Br$ displays limited reversibility under the 150 bar swing with isothermal entropy changes substantially lower than the full transition entropy: 74% of ΔS_{tr} (223 J K^{-1} kg^{-1}) and 58% of ΔS_{tr} (174 J K^{-1} kg^{-1}) for compression and decompression, respectively (Figure 6b,6e). Furthermore, the $\Delta S_{it,direct}$ values decreased upon cycling, ultimately approaching 33% ΔS_{tr} (compression) and 50% ΔS_{tr} (decompression). This result indicates that $(C_6)_2Br$ undergoes only partial phase transformations under these conditions, with the phase fraction available to transition decreasing after the first cycle (Figure S42). Consistent with the quasi-direct analysis predicting a limited temperature window for $\Delta S_{it,cyc}$ at 150 bar (Figure 5b), this experiment demonstrates that an operating pressure sufficiently larger than ΔP_{hys} is indeed required to fully drive reversible phase changes.

For $(C_6)_2Cl$ and $(C_6)_2I$, heat flow traces were plotted as a function of pressure to directly evaluate pressure hysteresis (Figure 7), which was calculated for each cycle as the difference in onset transition pressure (P_{tr}) between compression and decompression, with $\Delta P_{hys} = P_{tr,compression} - P_{tr,decompression}$. This evaluation reveals that pressure-driven phase transitions in $(C_6)_2Cl$ and $(C_6)_2I$ are associated with ΔP_{hys} of 59 and 58 bar, respectively. Intriguingly, these experimental ΔP_{hys} values are smaller than the ΔP_{hys} values of 76 bar (Cl) and 98 bar (I) calculated from isobaric HP-DSC measurements. We speculate that the difference in ΔP_{hys} mostly arises from extrinsic factors, such as deviations from isothermality and changes in the quality of thermal contact during the pressure cycle. Although further studies are needed to fully elucidate the origin of such differences, these results highlight the importance of using both isothermal and isobaric measurements to evaluate the potential of new barocaloric materials.

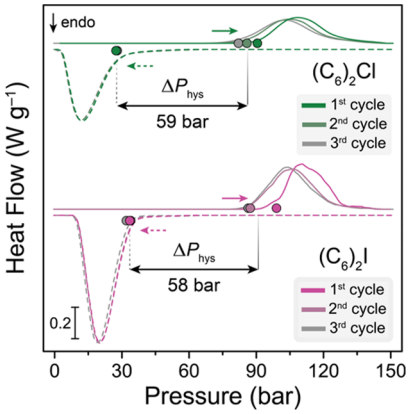

Figure 7. Heat flow signals from quasi-isothermal DSC experiments are plotted as a function of pressure for $(C_6)_2Cl$ (top) and $(C_6)_2I$ (bottom), with compression-induced exotherms (solid lines) and decompression-induced endotherms (dashed lines) obtained at average rates of 6 and 13 bar min^{-1}, respectively. Onset pressures for compression-induced exotherms and decompression-induced endotherms are indicated by circles. Pressure hysteresis, calculated as the difference between the onset pressures, is indicated by black arrows.

High-Pressure X-ray Diffraction and Raman Spectroscopy. Synchrotron PXRD and variable-pressure Raman spectroscopy measurements were used to extend the phase diagram for $(C_6)_2Br$, which has the highest entropy change of the dialkylammonium halide salts evaluated here, up to 1000 bar. Figure 8a shows a waterfall plot obtained for the PXRD patterns of $(C_6)_2Br$ collected from 360 to 220 K at 300 bar using He as the pressure-transmitting medium. As illustrated in the waterfall plot, the compound, initially in the high-entropy phase at 360 K, undergoes a phase transition to a contracted state upon cooling at 300 bar with an onset temperature of 296 K. Unit-cell parameters determined by Le Bail refinement show that the ordering transition is accompanied by a large anisotropic contraction of the lattice with $\Delta V_{tr}/V_{LT}$ of 10.4% (Figure S19), which is comparable to the volume change observed at ambient pressure.

Variable-pressure Raman spectroscopy experiments further show that this order−disorder transition persists at pressures as high as 900 bar. Specifically, Raman spectra were collected for a power sample of $(C_6)_2Br$ while pressurizing from 1 to 1000 bar and subsequently depressurizing to 1 bar at a constant temperature of 312 K. As depicted in Figure 8b, reversible transitions between ordered and disordered states were observed at 900 bar (compression) and 740 bar (decompression), the difference between which is in excellent agreement with the ΔP_{hys} of 149 bar predicted from HP-DSC experiments.

The transition onsets during the pressure-driven phase change were identified primarily by tracking C−H stretching modes. Peaks at 2920 and 2980 cm^{-1}—corresponding to symmetric and antisymmetric C−H stretches of the α-carbon—became more prominent and sharper upon the compression-induced ordering transition. Additionally, in the fingerprint region, a new peak emerged at 1340 cm^{-1} in the high-pressure ordered phase (Figure S44). DFT calculations indicate that this peak is associated with a wagging mode of N−H bonds (Figures S49 and S50). In addition to identifying phase boundaries at higher pressures, these results provide direct experimental evidence that the compression-induced ordering transition is accompanied by an enhancement of C−H···Br and N−H···Br interactions. This observation aligns with the Hirshfeld surface analyses based on computational structural models (Figure S9).

It is worth noting that the changes to C−H stretching vibrations observed during the transition are comparable to those observed in phase transitions in aqueous phospholipid dispersions and *n*-alkanes.[54] In addition, high-pressure Raman experiments used water as the pressure-transmitting medium. In contrast to 2D perovskites that typically degrade in water, this demonstrates that dialkylammonium halides are sufficiently hydrophobic for water to be used as a heat transfer fluid, which should provide valuable opportunities for thermal device engineering.[55] Most importantly, the transition onset temperatures and pressures determined from high-pressure PXRD and Raman spectroscopy are in excellent agreement with the extrapolated phase boundaries obtained by extending

https://doi.org/10.1021/jacs.3c12402
J. Am. Chem. Soc. XXXX, XXX, XXX−XXX

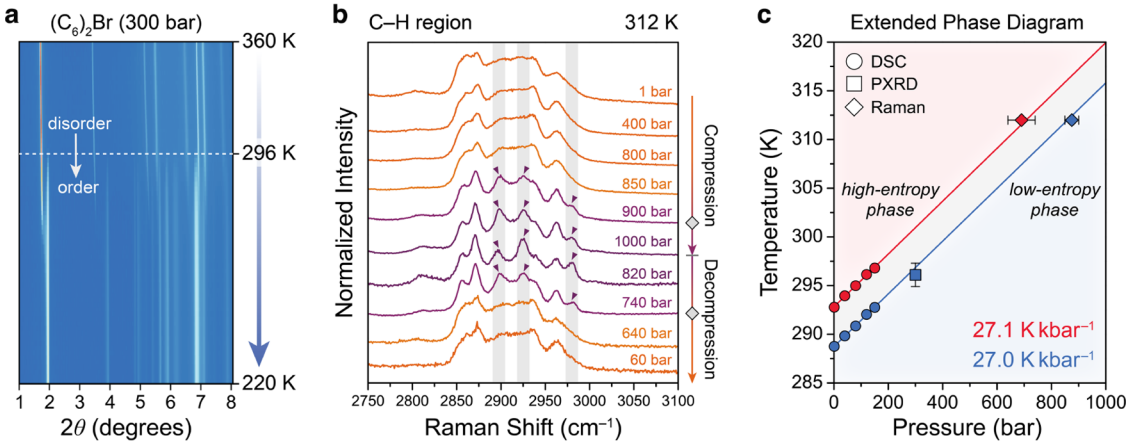

Figure 8. (a) Variable-temperature PXRD patterns for $(C_6)_2Br$ under 300 bar of He obtained during cooling with an X-ray wavelength of 0.45185 Å. The onset temperature for the ordering transition is indicated by a dashed line. (b) Variable-pressure Raman spectra, collected during a compression−decompression cycle between 1 and 1000 bar for $(C_6)_2Br$ at 312 K with water as the pressure-transmitting medium. The spectra for the C−H stretching region is shown, with onset pressures for compression-induced ordering and decompression-induced disordering transitions highlighted by gray circles. (c) High-pressure PXRD and Raman experiments extend the (P, T)-phase diagram for $(C_6)_2Br$ up to 1000 bar. Onset temperatures and pressures identified from PXRD and Raman experiments are in excellent agreement with the phase boundaries determined from isobaric HP-DSC.

the HP-DSC results at lower pressures (Figure 8c). As such, these experiments confirm that a pressure sensitivity of 27 K kbar^{-1} persists for $(C_6)_2Br$ even at much higher pressures and that the compound still undergoes a single transition between a low- and high-entropy state.

Nanocalorimetry. In addition to water compatibility, dialkylammonium halides have several other features that are advantageous for device applications. In particular, because of their solution-processable nature, they can be readily deposited onto a wide range of substrates as films with controllable thicknesses (Figure S53). Beyond device engineering, this offers a unique opportunity to characterize phase-change thermodynamics and kinetics through an array of advanced calorimetry techniques such as nanocalorimetry. Nanocalorimetry is a method that enables characterization of phase-change phenomena under extreme, nonequilibrium conditions and can allow for rapid thermal cycling tests to be performed.[56−58] Moreover, owing to its high sensitivity of near 1 nJ K^{-1}, the nanocalorimetry technique enables thermal characterization of thin-film samples at scan rates of up to 10^5 K s^{-1}.

To perform nanocalorimetry measurements, we first deposited a 50-nm-thick film of $(C_{10})_2Br$ [$(C_{10})_2$ = di-*n*-decylammonium] onto a nanocalorimetry sensor with an area of 1.9×10^{-2} cm^2. Note that the C_{10} analogue was used for these experiments instead of C_6 because its transition temperature (328 K) is above room temperature, which simplified the nanocalorimetry measurements. Due to the longer, more flexible C_{10} chain, $(C_{10})_2Br$ displays a phase-change entropy of 123 J mol^{-1} K^{-1} that is 54% higher than the molar ΔS_{tr} of $(C_6)_2Br$ (Table S5). This is consistent with the entire $(C_n)_2Br$ (n = 2−18) series of compounds for which the molar ΔS_{tr} values monotonically increase with increasing chain length (Figure S6). The order−disorder transition of $(C_{10})_2Br$ is also accompanied by a large volume change of 90.0 cm^3 kg^{-1} (9.6%) (Figure S21), which gives rise to a high pressure sensitivity of 23 K kbar^{-1} (Figure S37 and Table S8).

To allow for rapid scan rates, the thermal mass of the thin-film sample was kept very low (on the order of 100 ng). Interestingly, the phase transition temperature of $(C_{10})_2Br$ was 10 K lower for the thin-film sample compared to a bulk powder sample (Figure 9a), suggesting that the phase behavior of dialkylammonium halides can be influenced by size and substrate effects. This result has implications for the design and optimization of composite materials based on dialkylammonium halides and highlights the importance of exploring how sample size and morphology influence phase-change properties. Although further studies are needed to elucidate the origin

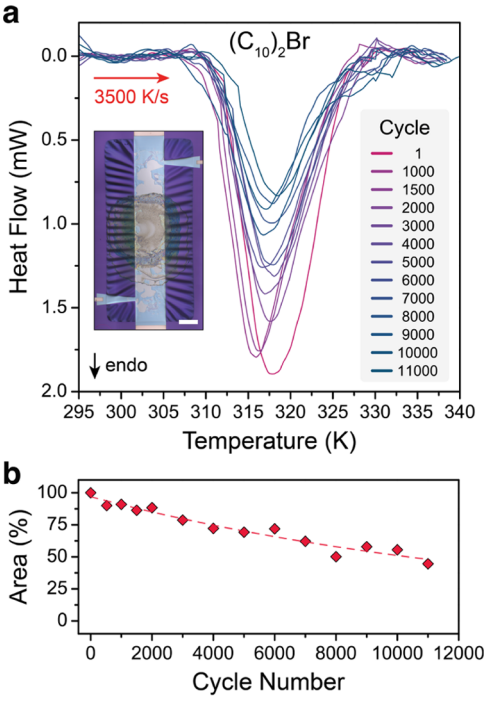

Figure 9. (a) Nanocalorimetry measurements for a thin-film sample of $(C_{10})_2Br$ with a heating rate of 3500 K s^{-1} over 11,000 cycles under high vacuum (10^{-5} Pa). An optical image of the sample deposited directly onto the nanocalorimetry sensor is displayed (scale bar = 500 μm). (b) Heating-induced endothermic transitions persisted throughout thermal cycling, but the transition peak area decreased due to sample sublimation under high vacuum.

https://doi.org/10.1021/jacs.3c12402
J. Am. Chem. Soc. XXXX, XXX, XXX−XXX

of this phenomenon, similar observations were previously made for martensitic transitions in alloy films[59,60] and spin transitions in molecular thin films.[61]

During over 11,000 thermal cycles with a heating scan rate of 3500 K s^{-1}, the phase transition temperature for $(C_{10})_2Br$ remained constant with onset and peak temperatures of 311 and 318 K, respectively. Note that a decrease in transition enthalpy was observed during thermal cycling, which is attributed to sample sublimation under the ultrahigh vacuum conditions (1.3×10^{-5} Pa) used for the nanocalorimetry experiments (Figure 9b). This was confirmed by optical images of the sensor area before and after cycling (Figures S56 and S57).

CONCLUSIONS

The foregoing results establish dialkylammonium halide salts as a new class of highly tunable barocaloric materials with excellent energy density, reversibility, processability, and stability. Through a systematic investigation of barocaloric effects in these organic materials, this work contributes to the rapidly growing knowledge base around pressure-induced phase transitions in organic salts,[37,62,63] long-chain hydrocarbons,[45,64−66] and plastic crystals.[67−69] Efforts to further investigate thermal conductivity, dynamics of disordered phases, and barocaloric effects across a wider range of soft materials are currently underway in our laboratory.

ASSOCIATED CONTENT

Supporting Information

The Supporting Information is available free of charge at https://pubs.acs.org/doi/10.1021/jacs.3c12402.

Additional experimental details, high-pressure calorimetry data, entropy curves used to evaluate barocaloric effects, powder X-ray diffraction data, single-crystal X-ray diffraction data, Raman spectroscopy data, and optical images and nanocalorimetry data, and a summary of all structural and thermodynamic data (PDF)

Accession Codes

CCDC 2171719−2171722 contain the supplementary crystallographic data for this paper. These data can be obtained free of charge via www.ccdc.cam.ac.uk/data_request/cif, or by emailing data_request@ccdc.cam.ac.uk, or by contacting The Cambridge Crystallographic Data Centre, 12 Union Road, Cambridge CB2 1EZ, UK; fax: +44 1223 336033.

AUTHOR INFORMATION

Corresponding Authors

Hao Yan − *Department of Chemistry, University of North Texas, Denton, Texas 76203, United States;* orcid.org/0000-0003-4894-5620; Email: hao.yan@unt.edu

Joost J. Vlassak − *John A. Paulson School of Engineering and Applied Sciences, Harvard University, Cambridge, Massachusetts 02138, United States*; Email: vlassak@seas.harvard.edu

Jarad A. Mason − *Department of Chemistry and Chemical Biology, Harvard University, Cambridge, Massachusetts 02138, United States;* orcid.org/0000-0003-0328-7775; Email: mason@chemistry.harvard.edu

Authors

Jinyoung Seo − *Department of Chemistry and Chemical Biology, Harvard University, Cambridge, Massachusetts 02138, United States;* orcid.org/0000-0002-3260-4963

Rahil Ukani − *Department of Chemistry and Chemical Biology, Harvard University, Cambridge, Massachusetts 02138, United States*

Juanjuan Zheng − *John A. Paulson School of Engineering and Applied Sciences, Harvard University, Cambridge, Massachusetts 02138, United States*

Jason D. Braun − *Department of Chemistry and Chemical Biology, Harvard University, Cambridge, Massachusetts 02138, United States;* orcid.org/0000-0002-5850-8048

Sicheng Wang − *Department of Chemistry, University of North Texas, Denton, Texas 76203, United States;* orcid.org/0000-0002-5224-5697

Faith E. Chen − *Department of Chemistry and Chemical Biology, Harvard University, Cambridge, Massachusetts 02138, United States*

Hong Ki Kim − *Department of Chemistry and Chemical Biology, Harvard University, Cambridge, Massachusetts 02138, United States;* orcid.org/0000-0002-6115-384X

Selena Zhang − *Department of Chemistry and Chemical Biology, Harvard University, Cambridge, Massachusetts 02138, United States*

Catherine Thai − *Department of Chemistry and Chemical Biology, Harvard University, Cambridge, Massachusetts 02138, United States;* orcid.org/0009-0002-6265-9903

Ryan D. McGillicuddy − *Department of Chemistry and Chemical Biology, Harvard University, Cambridge, Massachusetts 02138, United States*

Complete contact information is available at: https://pubs.acs.org/10.1021/jacs.3c12402

Notes

The authors declare the following competing financial interest(s): J.S., F.E.C., J.D.B., and J.A.M. are inventors of technology utilized in this research that is licensed to PasCal Technologies, Inc., of which J.S. and J.A.M. are Co-Founders. J.A.M is a Fiduciary Board member of PasCal Technologies, Inc. By improving upon the licensed technology, the outcomes of this research could result in a financial benefit to J.S, F.E.C, J.D.B, and J.A.M. and PasCal Technologies, Inc.

ACKNOWLEDGMENTS

This work was primarily supported by the Harvard MRSEC program of the National Science Foundation under award number DMR 20-11754. This research was also partially supported by the Climate Change Solutions Fund at Harvard University. This work was performed in part at the Harvard University Center for Nanoscale Systems (CNS); a member of the National Nanotechnology Coordinated Infrastructure Network (NNCI), which is supported by the National Science Foundation under NSF award number ECCS-2025158. X-ray diffraction data were collected on beamline 17-BM at the Advanced Photon Source at Argonne National Laboratory, which is supported by the U.S. Department of Energy, Office of Science, Office of Basic Energy Sciences under Contract No. DE-AC02-06CH11357. Part of this work was performed on Cruntch, the high-performance computing cluster at University of North Texas supported by the National Science Foundation under Awards OAC-2117247 and CHE-1531468. The authors

thank the IBS Center for Catalytic Hydrocarbon Functionalizations for allowing to use computational resources, Dr. Andrey A. Yakovenko for assisting with synchrotron PXRD experiments, Vidhya Dev for assisting with crystallographic analyses, and Kevin Miura for assisting with sample preparations. The authors also thank the Korea Foundation for Advanced Studies for a graduate fellowship awarded to J.S.

REFERENCES

(1) Cullen, W. Of the Cold Produced by Evaporating Fluids, and of Some Other Means of Producing Cold. In *Essays and Observations: Physical and Literary: Read Before a Society in Edinburgh, and Published by Them*; Hamilton, G.; Hamilton, G.; Balfour, J., Eds.; Hamilton and J. Balfour, 1756.

(2) Perkins, J. Apparatus and Means for Producing Ice and in Cooling Fluids. UK Patent GB6662/18351835.

(3) Bramwell, F. *One of the First Ice Machines*; Scientific American, 1883.

(4) ASME. *Perkins Vapor-Compression Cycle for Refrigeration*; History and Heritage Committee of the American Society of Mechanical Engineers, 2020.

(5) Harford, T. *Fifty Inventions That Shaped the Modern Economy*; Penguin, 2018.

(6) Dupont, J. L.; Domanski, P.; Lebrun, P.; Ziegler, F. *38th Note on Refrigeration Technologies: The Role of Refrigeration in the Global Economy*; International Institute of Refrigeration, 2019.

(7) IEA. *The Future of Cooling: Opportunities for Energy Efficient Air Conditioning*; International Energy Agency, 2018.

(8) IEA. *The Future of Heat Pumps*; International Energy Agency, 2022.

(9) McLinden, M. O.; Huber, M. L. (R)Evolution of Refrigerants. *J. Chem. Eng. Data* **2020**, *65* (9), 4176−4193.

(10) Flerlage, H.; Velders, G. J. M.; de Boer, J. A Review of Bottom-up and Top-down Emission Estimates of Hydrofluorocarbons (HFCs) in Different Parts of the World. *Chemosphere* **2021**, *283*, No. 131208.

(11) Coulomb, D.; Dupont, J. L.; Morlet, V. *35th Informatory Note on Refrigeration Technologies: The Impact of the Refrigeration Sector on Climate Change*; International Institute of Refrigeration, 2017.

(12) Velders, G. J. M.; Fahey, D. W.; Daniel, J. S.; McFarland, M.; Andersen, S. O. The Large Contribution of Projected HFC Emissions to Future Climate Forcing. *Proc. Natl. Acad. Sci. U.S.A.* **2009**, *106* (27), 10949−10954.

(13) McLinden, M. O.; Brown, J. S.; Brignoli, R.; Kazakov, A. F.; Domanski, P. A. Limited Options for Low-Global-Warming-Potential Refrigerants. *Nat. Commun.* **2017**, *8* (1), No. 14476.

(14) Midgley, T., Jr.; Henne, A. L. Organic Fluorides as Refrigerants. *Ind. Eng. Chem.* **1930**, *22* (5), 542−545.

(15) Molina, M. J.; Rowland, F. S. Stratospheric Sink for Chlorofluoromethanes: Chlorine Atom-Catalysed Destruction of Ozone. *Nature* **1974**, *249* (5460), 810−812.

(16) Burkholder, J. B.; Cox, R. A.; Ravishankara, A. R. Atmospheric Degradation of Ozone Depleting Substances, Their Substitutes, and Related Species. *Chem. Rev.* **2015**, *115* (10), 3704−3759.

(17) Wang, Z.; Wang, Y.; Li, J.; Henne, S.; Zhang, B.; Hu, J.; Zhang, J. Impacts of the Degradation of 2,3,3,3-Tetrafluoropropene into Trifluoroacetic Acid from Its Application in Automobile Air Conditioners in China, the United States, and Europe. *Environ. Sci. Technol.* **2018**, *52* (5), 2819−2826.

(18) Evich, M. G.; Davis, M. J. B.; McCord, J. P.; Acrey, B.; Awkerman, J. A.; Knappe, D. R. U.; Lindstrom, A. B.; Speth, T. F.; Tebes-Stevens, C.; Strynar, M. J.; Wang, Z.; Weber, E. J.; Henderson, W. M.; Washington, J. W. Per- and Polyfluoroalkyl Substances in the Environment. *Science* **2022**, *375* (6580), No. eabg9065.

(19) Polvani, L. M.; Previdi, M.; England, M. R.; Chiodo, G.; Smith, K. L. Substantial Twentieth-Century Arctic Warming Caused by Ozone-Depleting Substances. *Nat. Clim. Change* **2020**, *10* (2), 130−133.

(20) Western, L. M.; Vollmer, M. K.; Krummel, P. B.; Adcock, K. E.; Crotwell, M.; Fraser, P. J.; Harth, C. M.; Langenfelds, R. L.; Montzka, S. A.; Mühle, J.; O'Doherty, S.; Oram, D. E.; Reimann, S.; Rigby, M.; Vimont, I.; Weiss, R. F.; Young, D.; Laube, J. C. Global Increase of Ozone-Depleting Chlorofluorocarbons from 2010 to 2020. *Nat. Geosci.* **2023**, *16* (4), 309−313.

(21) Takeuchi, I.; Sandeman, K. Solid-State Cooling with Caloric Materials. *Phys. Today* **2015**, *68* (12), 48−54.

(22) Moya, X.; Mathur, N. D. Caloric Materials for Cooling and Heating. *Science* **2020**, *370* (6518), 797−803.

(23) Mañosa, L.; Planes, A. Solid-State Cooling by Stress: A Perspective. *Appl. Phys. Lett.* **2020**, *116* (5), No. 050501.

(24) Hou, H.; Qian, S.; Takeuchi, I. Materials, Physics and Systems for Multicaloric Cooling. *Nat. Rev. Mater.* **2022**, *7* (8), 633−652.

(25) Rodriquez, E. L.; Filisko, F. E. Thermoelastic Temperature Changes in Poly(Methyl Methacrylate) at High Hydrostatic Pressure: Experimental. *J. Appl. Phys.* **1982**, *53* (10), 6536−6540.

(26) Alex Müller, K.; Fauth, F.; Fischer, S.; Koch, M.; Furrer, A.; Lacorre, P. Cooling by Adiabatic Pressure Application in $Pr_{1-x}La_xNiO_3$. *Appl. Phys. Lett.* **1998**, *73* (8), 1056−1058.

(27) Boldrin, D. Fantastic Barocalorics and Where to Find Them. *Appl. Phys. Lett.* **2021**, *118* (17), No. 170502.

(28) Schipper, J.; Bach, D.; Mönch, S.; Molin, C.; Gebhardt, S. E.; Woellenstein, J.; Schaefer-Welsen, O.; Vogel, C.; Langebach, R.; Bartholomé, K. On the Efficiency of Caloric Materials in Direct Comparison with Exergetic Grades of Compressors. *J. Phys. Energy* **2023**, *5*, No. 045002.

(29) Seo, J.; McGillicuddy, R. D.; Slavney, A. H.; Zhang, S.; Ukani, R.; Yakovenko, A. A.; Zheng, S.-L.; Mason, J. A. Colossal Barocaloric Effects with Ultralow Hysteresis in Two-Dimensional Metal−Halide Perovskites. *Nat. Commun.* **2022**, *13* (1), No. 2536.

(30) Li, J.; Barrio, M.; Dunstan, D. J.; Dixey, R.; Lou, X.; Tamarit, J.-L.; Phillips, A. E.; Lloveras, P. Colossal Reversible Barocaloric Effects in Layered Hybrid Perovskite $(C_{10}H_{21}NH_3)_2MnCl_4$ under Low Pressure Near Room Temperature. *Adv. Funct. Mater.* **2021**, *31* (46), No. 2105154.

(31) Guillaume, F.; Coddens, G.; Dianoux, A. J.; Petry, W.; Rey-Lafon, M.; Sourisseau, C. Molecular Motions of Decylammonium Chains in the Perovskite Type Layered Compound $(C_{10}H_{21}NH_3)_2MnCl_4$. *Mol. Phys.* **1989**, *67* (3), 665−679.

(32) van Oort, M. J. M.; White, M. A. Polymorphism in Dialkylammonium Chlorides. An Adiabatic Calorimetry Study. *Ber. Bunsenges. Phys. Chem.* **1988**, *92* (2), 168−176.

(33) Steinert, S.; Voigt, W.; Glausch, R.; Neuschütz, M. Thermal Characteristics of Solid−Solid Phase Transitions in Long-Chain Dialkyl Ammonium Salts. *Thermochim. Acta* **2005**, *435* (1), 28−33.

(34) Whitman, C. A.; Johnson, M. B.; White, M. A. Characterization of Thermal Performance of a Solid−Solid Phase Change Material, Di-*n*-Hexylammonium Bromide, for Potential Integration in Building Materials. *Thermochim. Acta* **2012**, *531*, 54−59.

(35) Shimizu, T.; Tanaka, S.; Onoda-Yamamuro, N.; Ishimaru, S.; Ikeda, R. New Rotator Phase Revealed in Di-*n*-Alkylammonium Bromides Studied by Solid-State NMR, Powder XRD, Electrical Conductivity and Thermal Measurements. *J. Chem. Soc., Faraday Trans.* **1997**, *93* (2), 321−326.

(36) Nyburg, S. C. Di-*n*-Octadecylammonium Bromide. *Acta Crystallogr., Sect. C: Cryst. Struct. Commun.* **1996**, *52* (1), 192−194.

(37) García-Ben, J.; Bermúdez-García, J. M.; Dixey, R. J. C.; Delgado-Ferreiro, I.; Llamas-Saiz, A. L.; López-Beceiro, J.; Artiaga, R.; García-Fernández, A.; Cappel, U. B.; Alonso, B.; Castro-García, S.; Phillips, A. E.; Sánchez-Andújar, M.; Señarís-Rodríguez, M. A. Structure and Thermal Property Relationships in the Thermomaterial Di-*n*-Butylammonium Tetrafluoroborate for Multipurpose Cooling and Cold-Storage. *J. Mater. Chem. A* **2023**, *11* (41), 22232−22247.

(38) Oort, M. J. M.; White, M. A. General Trends in Phase Transitions in an Homologous Series. Polymorphism in $(n\text{-}C_6H_{13}NH_3)_2MnCl_4$ as Determined by Adiabatic Calorimetry from 18 to 313 K. *J. Chem. Soc., Faraday Trans. 1* **1985**, *81* (12), 3059−3065.

https://doi.org/10.1021/jacs.3c12402
J. Am. Chem. Soc. XXXX, XXX, XXX−XXX

(39) Sirota, E. B.; Singer, D. M.; King, H. E. Structural Effects of High Pressure Gas on the Rotator Phases of Normal Alkanes. *J. Chem. Phys.* **1994**, *100* (2), 1542−1551.
(40) Stammler, M. Polymorphism of Salts Containing Complex Ions—I: The Halides of Ammonium and Methyl-Substituted Ammonium. *J. Inorg. Nucl. Chem.* **1967**, *29* (9), 2203−2221.
(41) Lindgren, J.; Arran, N.; et al. Hydrogen Bond Studies. 62. The Crystal Structure of a High Temperature Modification of Dimethylammonium Chloride $(CH_3)_2NH_2Cl$: An X-Ray and Infrared Study. *Acta Chem. Scand.* **1972**, *26*, 3043−3052.
(42) Bellamy, L. J. *The Infrared Spectra of Complex Molecules*; Springer Netherlands: Dordrecht, 1980.
(43) Denis, P.-H.; Mertens, M.; Van Gompel, W. T. M.; Van Hecke, K.; Ruttens, B.; D'Haen, J.; Lutsen, L.; Vanderzande, D. Directing the Self-Assembly of Conjugated Organic Ammonium Cations in Low-Dimensional Perovskites by Halide Substitution. *Chem. Mater.* **2021**, *33* (13), 5177−5188.
(44) Würflinger, A.; Schneider, G. M. Differential Thermal Analysis under High Pressures II: Investigation of the Rotational Transition of Several *n*-Alkanes. *Ber. Bunsenges. Phys. Chem.* **1973**, *77* (2), 121−128.
(45) Poręba, T.; Kicior, I. Pressure-Freezing of Dodecane: Exploring the Crystal Structures, Formation Kinetics and Phase Diagrams for Colossal Barocaloric Effects in *n*-Alkanes. *RSC Adv.* **2023**, *13* (47), 33305−33317.
(46) Gutfleisch, O.; Gottschall, T.; Fries, M.; Benke, D.; Radulov, I.; Skokov, K. P.; Wende, H.; Gruner, M.; Acet, M.; Entel, P.; Farle, M. Mastering Hysteresis in Magnetocaloric Materials. *Philos. Trans. R. Soc., A* **2016**, *374* (2074), No. 20150308.
(47) Keller, A.; Cheng, S. Z. D. The Role of Metastability in Polymer Phase Transitions. *Polymer* **1998**, *39* (19), 4461−4487.
(48) Aznar, A.; Lloveras, P.; Barrio, M.; Negrier, P.; Planes, A.; Mañosa, L.; Mathur, N. D.; Moya, X.; Tamarit, J.-L. Reversible and Irreversible Colossal Barocaloric Effects in Plastic Crystals. *J. Mater. Chem. A* **2020**, *8* (2), 639−647.
(49) Hess, T.; Maier, L. M.; Bachmann, N.; Corhan, P.; Schäfer-Welsen, O.; Wöllenstein, J.; Bartholomé, K. Thermal Hysteresis and Its Impact on the Efficiency of First-Order Caloric Materials. *J. Appl. Phys.* **2020**, *127* (7), No. 075103.
(50) Masche, M.; Ianniciello, L.; Tušek, J.; Engelbrecht, K. Impact of Hysteresis on Caloric Cooling Performance. *Int. J. Refrig.* **2021**, *121*, 302−312.
(51) Song, Y.; Chen, X.; Dabade, V.; Shield, T. W.; James, R. D. Enhanced Reversibility and Unusual Microstructure of a Phase-Transforming Material. *Nature* **2013**, *502* (7469), 85−88.
(52) Moya, X.; Kar-Narayan, S.; Mathur, N. D. Caloric Materials near Ferroic Phase Transitions. *Nat. Mater.* **2014**, *13* (5), 439−450.
(53) Seo, J.; Braun, J. D.; Dev, V. M.; Mason, J. A. Driving Barocaloric Effects in a Molecular Spin-Crossover Complex at Low Pressures. *J. Am. Chem. Soc.* **2022**, *144* (14), 6493−6503.
(54) Wong, P. T. T. Raman Spectroscopy of Thermotropic and High-Pressure Phases of Aqueous Phospholipid Dispersions. *Annu. Rev. Biophys. Bioeng.* **1984**, *13* (1), 1−24.
(55) Rohsenow, W. M.; Hartnett, J. P.; Ganic, E. N. *Handbook of Heat Transfer Applications*, 2nd ed.; McGraw-Hill, 1985.
(56) Zheng, J.; Miao, Y.; Zhang, H.; Chen, S.; Lee, D.; Arróyave, R.; Vlassak, J. J. Phase Transformations in Equiatomic CuZr Shape Memory Thin Films Analyzed by Differential Nanocalorimetry. *Acta Mater.* **2018**, *159*, 320−331.
(57) McCluskey, P. J.; Vlassak, J. J. Combinatorial Nanocalorimetry. *J. Mater. Res.* **2010**, *25* (11), 2086−2100.
(58) Gregoire, J. M.; Xiao, K.; McCluskey, P. J.; Dale, D.; Cuddalorepatta, G.; Vlassak, J. J. *In-Situ* X-Ray Diffraction Combined with Scanning AC Nanocalorimetry Applied to a $Fe_{0.84}Ni_{0.16}$ Thin-Film Sample. *Appl. Phys. Lett.* **2013**, *102* (20), No. 201902.
(59) Zhang, Y.; Billman, J.; Shamberger, P. J. Size Effects in the Martensitic Transformation Hysteresis in Ni−Mn−Sn Heusler Alloy Films. *Acta Mater.* **2019**, *180*, 116−125.
(60) Wang, X.; Vlassak, J. J. Thickness and Film Stress Effects on the Martensitic Transformation Temperature in Equi-Atomic NiTi Thin Films. *Mech. Mater.* **2015**, *88*, 50−60.
(61) Shalabaeva, V.; Mikolasek, M.; Manrique-Juarez, M. D.; Bas, A.-C.; Rat, S.; Salmon, L.; Nicolazzi, W.; Molnár, G.; Bousseksou, A. Unprecedented Size Effect on the Phase Stability of Molecular Thin Films Displaying a Spin Transition. *J. Phys. Chem. C* **2017**, *121* (45), 25617−25621.
(62) Ren, Q.; Qi, J.; Yu, D.; Zhang, Z.; Song, R.; Song, W.; Yuan, B.; Wang, T.; Ren, W.; Zhang, Z.; Tong, X.; Li, B. Ultrasensitive Barocaloric Material for Room-Temperature Solid-State Refrigeration. *Nat. Commun.* **2022**, *13* (1), No. 2293.
(63) Yu, C.; Huang, J.; Qi, J.; Liu, P.; Li, D.; Yang, T.; Zhang, Z.; Li, B. Giant Barocaloric Effects in Formamidinium Iodide. *APL Mater.* **2022**, *10* (1), No. 011109.
(64) Lin, J.; Tong, P.; Zhang, K.; Tao, K.; Lu, W.; Wang, X.; Zhang, X.; Song, W.; Sun, Y. Colossal and Reversible Barocaloric Effect in Liquid-Solid-Transition Materials *n*-Alkanes. *Nat. Commun.* **2022**, *13* (1), No. 596.
(65) Zhang, C.; Wang, D.; Qian, S.; Zhang, Z.; Liang, X.; Wu, L.; Long, L.; Shi, H.; Han, Z. Giant Barocaloric Effects with a Wide Refrigeration Temperature Range in Ethylene Vinyl Acetate Copolymers. *Mater. Horiz.* **2022**, *9* (4), 1293−1298.
(66) Miliante, C. M.; Christmann, A. M.; Soares, R. P.; Bocca, J. R.; Alves, C. S.; Carvalho, A. M. G.; Muniz, A. R. On the Colossal Barocaloric Effect in Higher *n*-Alkanes. *J. Mater. Chem. A* **2022**, *10* (15), 8344−8355.
(67) Li, B.; Kawakita, Y.; Ohira-Kawamura, S.; Sugahara, T.; Wang, H.; Wang, J.; Chen, Y.; Kawaguchi, S. I.; Kawaguchi, S.; Ohara, K.; Li, K.; Yu, D.; Mole, R.; Hattori, T.; Kikuchi, T.; Yano, S.; Zhang, Z.; Zhang, Z.; Ren, W.; Lin, S.; Sakata, O.; Nakajima, K.; Zhang, Z. Colossal Barocaloric Effects in Plastic Crystals. *Nature* **2019**, *567* (7749), 506−510.
(68) Lloveras, P.; Aznar, A.; Barrio, M.; Negrier, P.; Popescu, C.; Planes, A.; Mañosa, L.; Stern-Taulats, E.; Avramenko, A.; Mathur, N. D.; Moya, X.; Tamarit, J.-L. Colossal Barocaloric Effects near Room Temperature in Plastic Crystals of Neopentylglycol. *Nat. Commun.* **2019**, *10* (1), No. 1803.
(69) Das, S.; Mondal, A.; Reddy, C. M. Harnessing Molecular Rotations in Plastic Crystals: A Holistic View for Crystal Engineering of Adaptive Soft Materials. *Chem. Soc. Rev.* **2020**, *49* (24), 8878−8896.

NOTE ADDED AFTER ASAP PUBLICATION

CCDC codes were inadvertently omitted in the version published January 16, 2024 and were correctly restored January 18, 2024.

https://doi.org/10.1021/jacs.3c12402
J. Am. Chem. Soc. XXXX, XXX, XXX−XXX